THE ROYAL SOCIETY

Dependence of the direct dislocation image on sample-to-film distance in X-ray topography

By X. R. Huang, M. Dudley, J. Y. Zhao and B. Raghothamachar

Department of Materials Science and Engineering, State University of New York at Stony Brook, Stony Brook, NY 11794-2275, USA

The geometrical diffraction model is used to simulate superscrew dislocation images both on characteristic radiation and synchrotron radiation topographs. It is revealed that, due to the finite spectrum width, characteristic radiation diffraction occurring in the deformed lattice of a dislocation also belongs to polychromatic diffraction. The contrast formation mechanisms of characteristic radiation topography are thus almost identical to that of synchrotron white-beam topography. As a general rule, the dimensions of dislocation images increase drastically with increasing sample-to-film distances, making the characteristic radiation images recorded at short sample-to-film distances much smaller than the synchrotron radiation images recorded at large distances.

Keywords: X-ray topography; dislocation image; imaging distance; back reflection; superscrew dislocation

1. Introduction

In contrast to synchrotron radiation, which has a continuous spectrum and natural collimation, characteristic radiation emitted from the conventional X-ray generator is a nearly monochromatic but divergent beam. For X-ray topography, the different source properties have usually been considered to be the main factor which gives rise to different contrast features of the same defect on the characteristic radiation topograph and on the synchrotron white-beam topograph. A general difference between these two kinds of topograph is that the defect image is usually much wider on the synchrotron topograph than on the characteristic radiation topograph recorded at the same Bragg angle. In the literature, the wider image on the synchrotron topograph was mostly explained to result from the high-order harmonic reflections which, according to the conventional theory, have long extinction distances and can significantly increase the direct image widths (Tanner (1996) and references therein).

Indeed, the increase of the image width with decreasing X-ray wavelength can be readily revealed on topographs taken by X-rays of different wavelengths. Using Lang topography, Klapper (1991) has shown that the average image width of screw dislocations obtained by MoKα radiation is much wider than that obtained by CuKα radiation for the same reflection. Zontone *et al*. (1996) demonstrated that in the short-wavelength range, the direct dislocation images on synchrotron topographs are extremely wide. They also showed that the image width as a function of wavelength is not a monotonic function, but shows abrupt jumps as the long-wavelength reflections

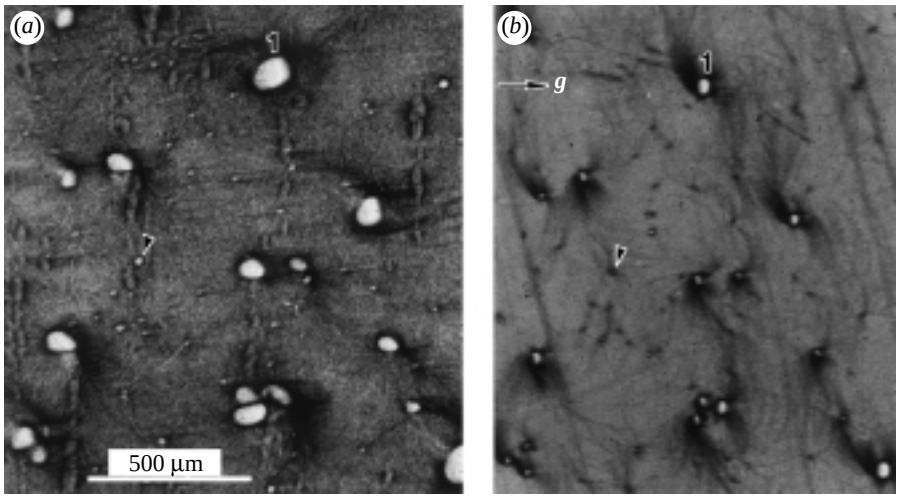

Figure 1. Back-reflection images (white spots surrounded by black contrast) of superscrew dislocations in 6H–SiC. (*a*) Synchrotron radiation topograph. Main reflections 00018 ($\lambda = 1.65$ Å) and 00024 ($\lambda = 1.25$ Å), sample-to-film distance $D = 10$ cm. (*b*) Lang topograph (back reflection), 00018 reflection, CuKα_1 radiation ($\lambda = 1.541$ Å), $D = 2$ cm. The irregular black streaks surrounding the white dots are basal plane dislocation images.

are strongly absorbed and the short-wavelength harmonics successively dominate the image.

Although the influence of wavelength on the image width can qualitatively explain the difference between some topographic contrast features on Lang and synchrotron topographs, inconsistency can be found on reflection topographs where the low-order reflections dominate the image. For example, figures $1a, b$ are two back-reflection topographs of a (0001) 6H–SiC wafer taken by synchrotron radiation and CuKα_1 radiation, respectively, showing that the synchrotron radiation images of the so-called 'superscrew dislocations' (Dudley *et al*. 1995) are still significantly wider than the CuKα_1 radiation images. The difference here clearly indicates that the dimension variation of dislocation images cannot be solely attributed to the different wavelengths of the diffracted X-rays.

In this paper, we will show that apart from the influence of wavelength, the dominant factor determining the direct dislocation image width on X-ray topographs is the sample-to-film distance. In fact, from our simple treatment for the geometrical diffraction of superscrew dislocations in 6H–SiC, we will illustrate that regardless of harmonic reflections, the contrast formation mechanisms of characteristic radiation topography are nearly identical to those of synchrotron white-beam topography. The different contrast features between these two kinds of topographs mainly arise from the different sample-to-film distances used. Therefore, characteristic radiation topography and synchrotron topography can be regarded as two supplementary techniques which cover the imaging distances from a few millimetres to tens of centimetres.

2. Geometrical diffraction image of superscrew dislocation

In our previous work (Huang *et al*. 1999*a*, *b*; Dudley *et al*. 1999) we have demonstrated that a simple geometrical diffraction model can be used to simulate the main

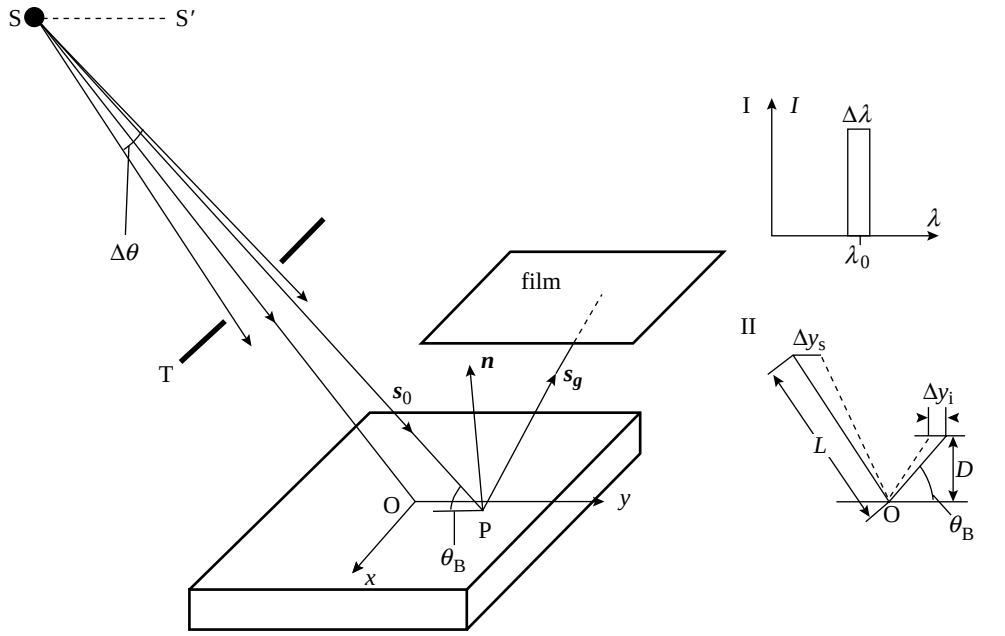

Figure 2. Schematic of the symmetric back-reflection geometry. Inset I represents the spectrum profile used in the simulations of characteristic radiation topographs. Inset II shows the image displacement arising from the source shift (diffusion effect) in characteristic radiation topography.

contrast features of dislocations on synchrotron topographs. In this model, the distorted lattice around a dislocation is assumed to consist of a large number of small crystallites which are misoriented by the strain field and diffract X-rays independently according to their local lattice orientations. The simulation procedure based on this model is very simple for synchrotron topography as the incident radiation may be considered as a parallel beam with its slight divergence being neglected. Thus, the deviations of the local Bragg angles result solely from the orientation variation of the diffracting planes in the long-range strain field of the dislocation. For characteristic radiation topography, however, the finite divergence of the incident beam has to be considered according to the actual diffraction conditions.

For simulation of characteristic radiation topographs, the simplest case is that the X-ray source is a point source (Schulz method (Schulz 1954)). Figure 2 represents schematically the symmetric back-reflection geometry of this method. In this geometry, it should be noted that considering the incident beam as an ideal monochromatic beam would lead to a situation where only a narrow ribbon-like region (several micrometres in width) of the sample can diffract X-rays. This is because the Bragg angle θ_B changes slightly from point to point in the crystal, and only in the narrow region is the deviation of θ_B from the ideal Bragg angle within the rocking-curve range. (In previous simulations of section topographs or even Lang topographs using the Taupin–Takagi equations (Epelboin 1985, 1996), the incident beam was indeed treated as a spherical monochromatic wave, but a significant approximation made there was that the point source was assumed to lie on the entrance surface. This assumption is based on the fact that a polychromatic beam is, to some extent, equiva-

lent to a monochromatic but divergent beam. However, this equivalence is not always true.) Therefore, we have to take into account the finite width of the characteristic radiation spectrum. For CuKα_1 radiation ($\lambda_0 = 1.541$ Å), the FWHM width of the spectrum, $\Delta\lambda$, is about 4.9×10^{-4} Å (Deutsch & Hart 1982). In the 00018 reflection of 6H–SiC, this value corresponds to an angular width $\Delta\theta_\lambda = 7.15 \times 10^{-4}$ rad which is far greater than the rocking-curve width, 1.56×10^{-5} rad (Vetter & Dudley 1998). In the following, we will simply assume that the spectrum has a flat intensity profile within the wavelength range from $\lambda_0 - \frac{1}{2}\Delta\lambda$ to $\lambda_0 + \frac{1}{2}\Delta\lambda$ and outside this range the intensity falls to zero (see inset I of figure 2).

In order to simulate the superscrew dislocation images taken under the diffraction conditions of figure 1*a*, let us consider in figure 2 that a screw dislocation perpendicularly intersects the crystal surface at O with both the dislocation line and the Burgers vector $\boldsymbol{b}$ parallel to the z-axis. Under this condition, the position-dependent normal $\boldsymbol{n}$ to the (00018) diffracting plane can be obtained from the displacement field $u_z = (b/2\pi)\tan^{-1}(y/x)$ (Huang *et al.* 1999*b*). Let the incident direction of an arbitrary point P(x, y) on the crystal surface be $\boldsymbol{s}_0$ (a unit vector along SP) which is also slightly position dependent. Then the direction of the diffracted X-rays from P is

$$\boldsymbol{s}_g = \boldsymbol{s}_0 + 2\sin\theta_\mathrm{B}\boldsymbol{n} \tag{2.1}$$

in the symmetric back reflection, where $\sin\theta_\mathrm{B} = -\boldsymbol{s}_0 \cdot \boldsymbol{n}$. The wavelength of the diffracted X-rays can be obtained from

$$\frac{2\sin\theta_\mathrm{B}}{|\boldsymbol{g}_0 - \nabla(\boldsymbol{g}_0 \cdot \boldsymbol{u})|} = \lambda, \tag{2.2}$$

where $\boldsymbol{g}_0 - \nabla(\boldsymbol{g}_0 \cdot \boldsymbol{u})$ is the modified diffraction vector at P and $\boldsymbol{g}_0$ is the principal diffraction vector of the perfect lattice.

In the actual simulation process, we have to divide the crystal surface into a set of small squares and then calculate the direction $\boldsymbol{s}_g$ for each square. Neglecting the possible variation of diffraction ability in the deformed lattice, we can further assume that the squares whose diffraction wavelengths satisfy $|\lambda - \lambda_0| \leqslant \frac{1}{2}\Delta\lambda$ have the same diffraction intensity, while the others diffract negligible intensities. (More rigorous treatments would require one to consider the detailed intensity distribution of the spectrum and even the variation of diffraction ability from point to point in the strain field.) By projecting the intensities along the ray traces onto the recording plate, we may obtain the inhomogeneous intensity distribution (orientation contrast) on the film.

According to our previous calculations (Huang *et al.* 1999*b*) we can estimate that the Burgers vector magnitudes of dislocation 1 in figure 1*a* is around 20c ($c = 15.17$ Å is the lattice constant along the c-axis of 6H–SiC). In the following, we will mainly describe the simulations of the 20c superscrew dislocation.

Figure 3*a* is the CuKα_1 radiation image of a 20c superscrew dislocation simulated on the basis of the above principles. In simulating this image, we have chosen the source-to-sample distance L to be 2 m and the sample-to-film distance D to be 2 cm according to our experimental conditions (Vetter & Dudley 1998). The simulated image is an elliptical white spot surrounded by black contrast. The difference between this image and the recorded images in figure 1*b* results because figure 1*b* is a Lang topograph.

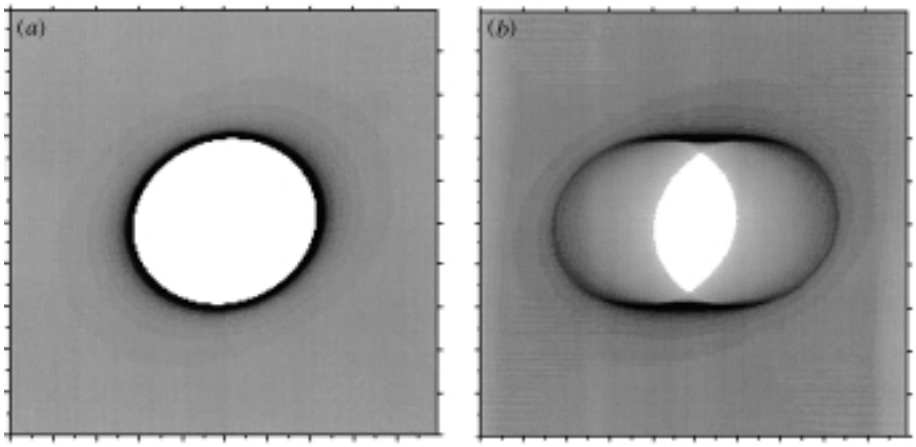

Figure 3. Simulated back-reflection images of a $20c$ superscrew dislocation with CuKα_1 radiation, 00018 reflection and $D = 2$ cm: (a) image obtained from a point source; (b) Lang topographic image with beam divergence 10^{-3} rad. Image size is $100 \times 100\ \mu m^2$.

It is noticeable that in inset II of figure 2, if the point source S is displaced by a distance Δy_s along SS′ (a line parallel to the y-axis), the simultaneous displacement of the diffraction image will be

$$\Delta y_i = -\frac{\Delta y_s D}{L \sin \theta_B}. \tag{2.3}$$

For the perfect lattice, such an image displacement is possible only when $|\Delta y_s| \leqslant L\Delta\lambda/(2d \sin 2\theta_B)$, where d is the spacing of the diffracting planes. Outside this range ($2|\Delta y_s| \leqslant 1.56$ mm and $2|\Delta y_i| \leqslant 17\ \mu$m for the present 00018 reflection of 6H–SiC), the diffraction wavelength moves out of the narrow spectrum and little intensity is diffracted. For the continuously deformed lattice, however, even if the principal diffraction wavelength moves out of the spectrum, it is possible that the wavelengths of some locally diffracted X-rays still satisfy $|\lambda - \lambda_0| < \frac{1}{2}\Delta\lambda$. Therefore, the maximum image displacement for a deformed lattice is usually larger than that for a perfect lattice, as will be shown in the following case of Lang topography. The possible image displacement implies that the size of the source in Schulz topography should be kept very small to avoid image diffusion. For instance, as the ratio D/L in our present case is 0.01, the source size should be less than 0.2 mm to achieve a resolution of 2 μm.

With some modifications, the simulation method for the point-source diffraction can be easily extended to simulate Lang topographs. In Lang topography, the simultaneous scanning of the sample and the recording film is equivalent to the scanning of the X-ray source alone, with the sample and the film being fixed. Thus, the source may be considered to consist of a set of point sources located on the line SS′ in figure 2. In this case, the slit T, which is indispensable in the actual experiment, plays an important role: it limits the divergence of the incident beam down to 10^{-3}–10^{-4} rad in the incident plane and more importantly, makes the 'diffusion effect' resulting from the finite source size very small.

The slit we used to take the Lang topograph of figure 1b is 1.5 mm wide, located about 2 m away from a fine focus source of 0.4 mm in size. From this condition it is estimated that the divergence of the X-ray beam is about 10^{-3} rad in the incidence

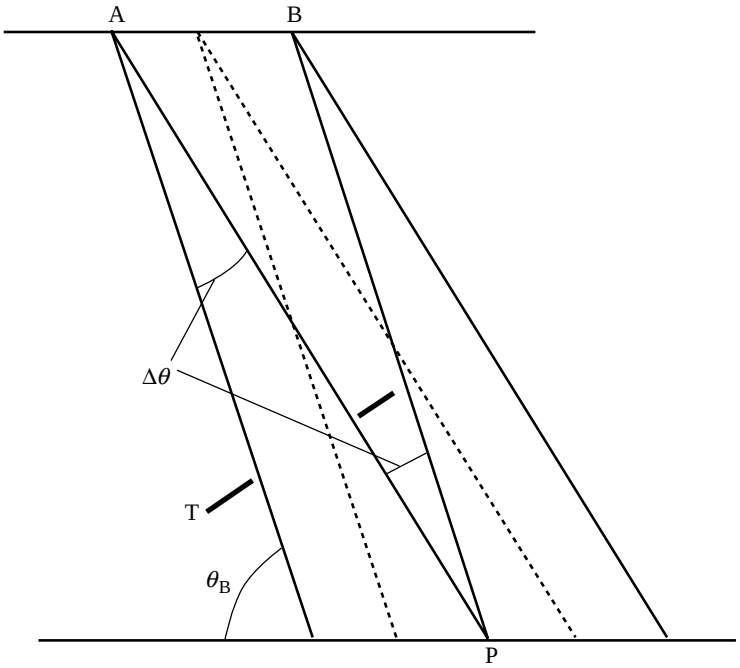

Figure 4. Schematic representation of the 'finite source size' in Lang topography, which gives rise to the 'diffusion effect'. $\Delta\theta$ is the divergence of the incident beam and T is the divergence-controlling slit.

plane. Since the perpendicular divergence (along the x-direction in figure 2) is not limited, the incident X-rays can be treated as a wedge-shaped beam. Scanning such a beam along the line SS′ and using the above simulation method, we have simulated the Lang topographic image of a 20c superscrew dislocation which is plotted in figure 3b. It is apparent that the image in figure 3b is smaller than that in figure 3a, but is closer to the recorded images in figure 1b. Here it is shown that the aforementioned diffusion effect does influence the dislocation contrast on the Lang topograph.

The diffusion effect in Lang topography may be understood from the schematic diagram in figure 4. During the scanning process, a point P on the crystal surface is irradiated by the wedge-shaped incident beam only when the source is between A and B. Thus, the 'effective source size' is $\Delta y_{\mathrm{s}} = \overline{\mathrm{AB}} = L\Delta\theta/\sin\theta_{\mathrm{B}}$, or 2.2 mm in our experiments. Based on equation (2.3), this size leads to a diffusion length $|\Delta y_{\mathrm{i}}| = 24\,\mu\mathrm{m}$, which is actually the diameter difference between the two images in figure 3 along the horizontal direction. Therefore, if the horizontal diameter of the white contrast centre image is less than 24 μm in the ideal point source topograph, the white centre will disappear on the Lang topograph, but a light contrast stripe sandwiched by two black lines will be observed (see the images marked by arrows in figure 1b).

3. Dependence of image width on sample-to-film distance

The diffusion effect on Lang topographs becomes negligible when the incidence divergence is controlled in the order of 10^{-4} rad. In experiments, this condition could be

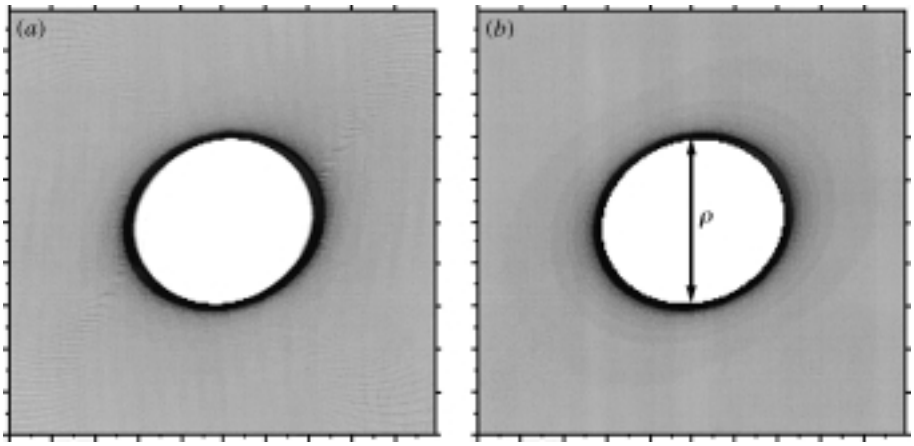

Figure 5. (*a*) Simulation of a 20*c* superscrew dislocation image. The simulation conditions are the same as those of figure 3*b* except that the beam divergence is 10^{-4} rad. (*b*) The corresponding image obtained from a parallel white beam. Image size $100 \times 100\ \mu m^2$.

achieved by use of sub-millimetre slits although the exposure time would be significantly prolonged. Figure 5*a* is the 20*c* superscrew dislocation image simulated with the divergence of the incident beam being exactly 10^{-4} in the incidence plane. Now the diameter of the white centre is almost the same as that of figure 3*a* since the diffusion length here is 2.4 μm, which is below the resolution limit of most X-ray films or plates.

It is interesting that under the same diffraction geometry (especially at the same sample-to-film distance), the superscrew dislocation image simulated by a totally parallel white beam also has the same contrast features (including both the intensity distribution and the image dimension) as those in figures 3*a* and 5*a*. Such a simulation is plotted in figure 5*b*. Moreover, by assuming that the parallel beam has the same spectrum width as CuKα_1, we have found that the simulated image has no observable change with respect to figure 5*b*. This indicates that during the white-beam imaging process, most of the X-rays undergoing diffraction are those whose wavelengths are within a narrow band, with the bandwidth comparable with the spectrum width of CuKα_1 radiation. In other words, although the spectrum width of characteristic radiation is very narrow, the source still provides a 'white beam' for diffraction in the deformed lattice in the characteristic radiation imaging process.

Thus, the contrast formation mechanisms of characteristic radiation topography are very similar to those of synchrotron white-beam topography. Regardless of the harmonic reflections of synchrotron topography, the only difference is that the diffracted beam in characteristic radiation topography has an extra divergence arising from the divergence of the incident beam, but this extra divergence is much smaller than that arising from the variation of the diffraction vector in the inhomogeneously deformed lattice. As the sample is very close to the film, the extra divergence has little influence on the contrast features.

Therefore, under the condition that the diffusion effect is well controlled, a Lang or Schulz topograph may be regarded simply as a white-beam topograph recorded at a short sample-to-film distance. Actually, synchrotron white-beam topographs are usually taken at sample-to-film distances not less than 10 cm (in order to avoid image

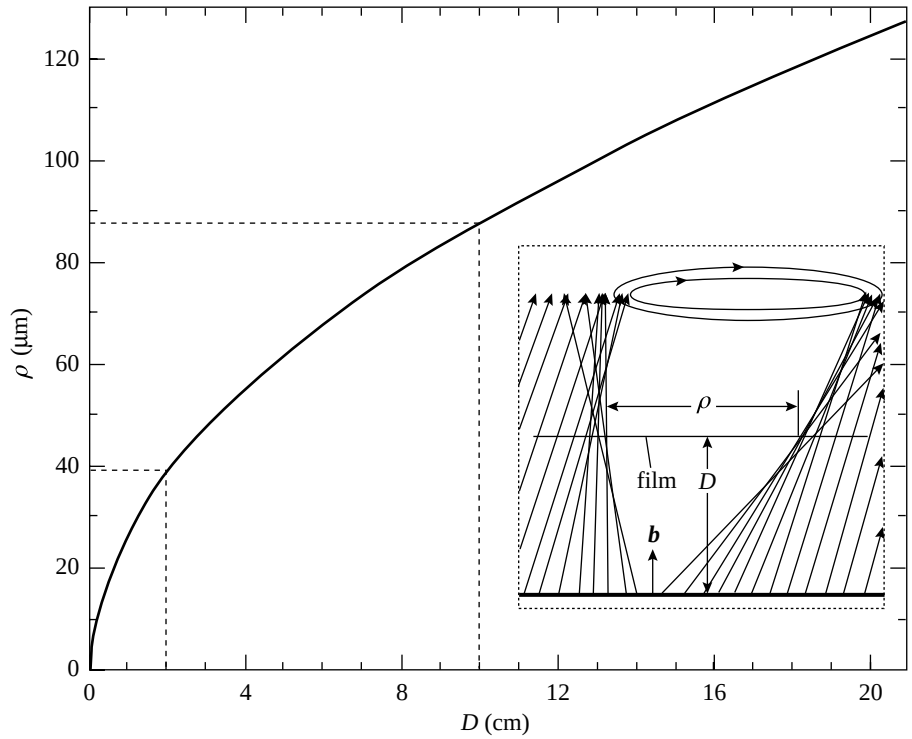

Figure 6. Dependence of the vertical diameter ρ (see figure 5*b*) on the sample-to-film distance D. Calculation parameters: 00018 reflection, parallel beam, principal Bragg angle 66°, $|\boldsymbol{b}| = 20c$. Inset shows the cross-sectional configurations of the twisted diffraction cones.

overlap and the influence of the direct beam), while Lang topographs are generally recorded at sample-to-film distances around a few centimetres (in order to maintain good spatial resolution). Thus, we can see that the main factor giving rise to the different contrast features on the two kinds of topographs is the different sample-to-film distances used.

Since the small divergence of the incident beam does not play an important role in the imaging process, we can simply use a parallel beam to calculate the dependence of the image diameter on the sample-to-film distance. Figure 6 shows the calculated diameters ρ of the back-reflection superscrew dislocation images at different sample-to-film distances, in which the diameter increases significantly but nonlinearly with increasing sample-to-film distances. In fact, this dependence has been tested in our synchrotron topography experiments from 4–30 cm, and the measured data are in good agreement with the calculated results. For example, the diameter value of 88 μm calculated at $D = 10$ cm is consistent with the vertical diameter of dislocation 1 in figure 1*b*. Here it should be mentioned that the Bragg angle of figure 1*b* ($\theta_B = 80°$) is different from that used in our calculations. As can be easily verified, however, such a difference does not affect the image diameter along the vertical direction (perpendicular to the incidence plane). In the short sample-to-film distance range where it is very difficult to take synchrotron topographs, the dependence curve in figure 6 may be verified by Lang topography with a well-collimated incident beam.

In our previous work (Huang *et al*. 1999*b*) we have demonstrated that in the

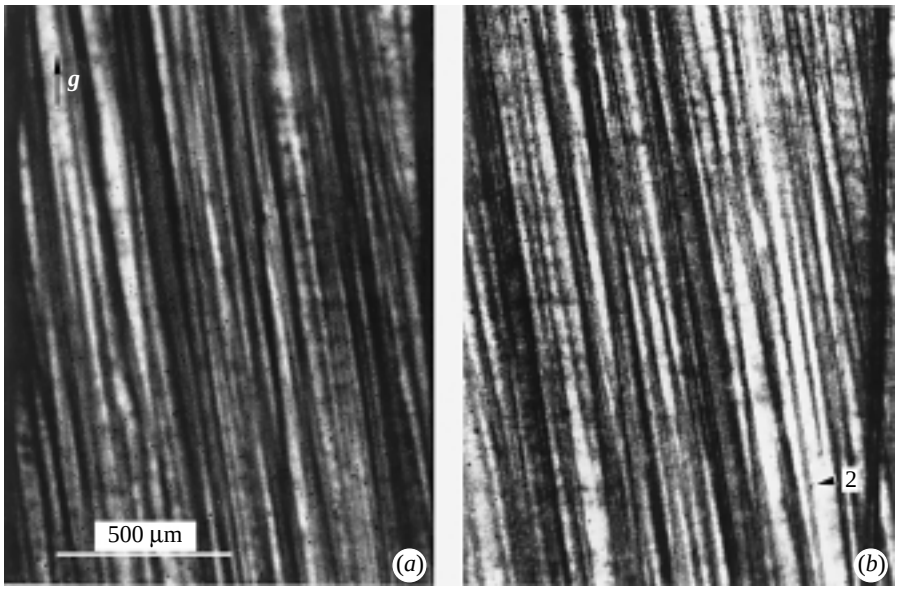

Figure 7. Transmission topographic images of superscrew dislocations in a $(11\bar{2}0)$ 6H–SiC wafer with 0006 reflection. (*a*) Synchrotron topograph with $D = 10$ cm. Note that the wide double-contrast images heavily overlap each other so that they can hardly be distinguished. (*b*) Lang topograph with CuKα_1 radiation and $D = 2$ cm.

symmetric back-reflection geometry, X-rays diffracted from different circles around the superscrew dislocation actually form a set of twisted cones. The inset of figure 6 shows schematically the cross-sectional configurations of these cones in space. From this diagram it is easy to understand the contrast formation mechanism and the dependence of the image diameter on the sample-to-film distance.

The drastic difference between the superscrew dislocation images on Lang and synchrotron topographs can also be revealed in the transmission geometry. Figures 7*a*, *b* are two transmission topographs of a $(11\bar{2}0)$ 6H–SiC wafer taken by CuKα_1 radiation and synchrotron radiation, respectively. In this case, the superscrew dislocations in the wafer are generally parallel to the surfaces, and their images on the topographs are the typical double-contrast images (see the individual dislocation 2 in figure 1*b*). Again, such image features can be strictly simulated by the above geometrical diffraction model, and our detailed calculations and measurements show that the dependence of the separation between the two intensity maxima on the sample-to-film distance is very similar to that of the back-reflection case (Huang *et al*. 1999*b*).

4. Discussion and conclusion

The above demonstrations of the similarities between characteristic radiation topography and synchrotron white-beam topography are based on the geometrical diffraction model, which has been described in detail in our previous work (Dudley *et al*. 1999). This model only takes into account the continuously varying directions of the diffracted X-rays resulting from the continuously varying directions of the deformed lattices around the dislocation, and the topographic contrast calculated is pure orien-

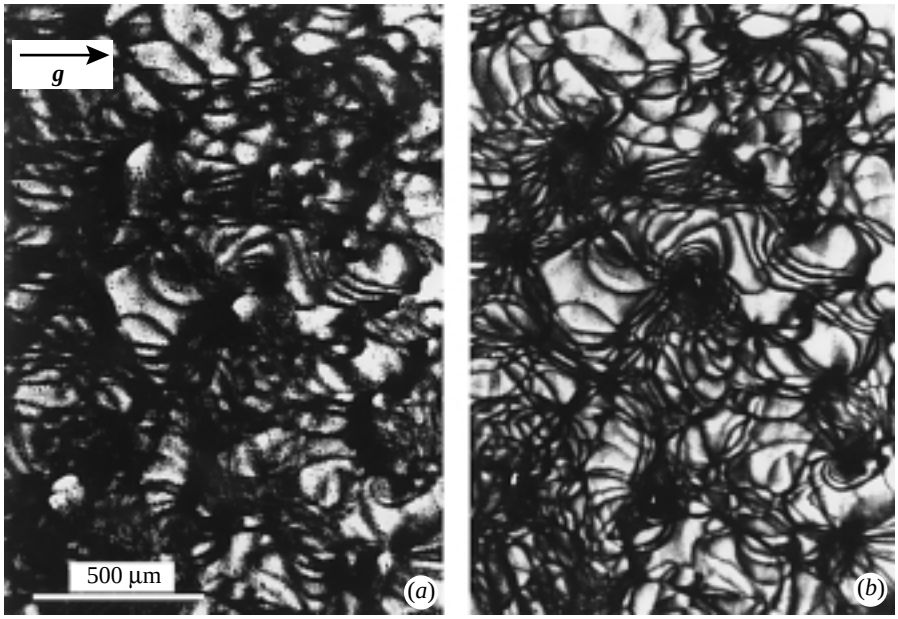

Figure 8. Transmission topographic images of basal plane dislocations in 6H–SiC with a (0001) wafer and $11\bar{2}0$ reflection: (*a*) synchrotron topograph with $D = 10$ cm; (*b*) Lang topograph with CuKα_1 radiation and $D = 2$ cm.

tation contrast originated from the overlap and separation of the diffracted X-rays on the topograph. Therefore, this model is unable to describe the possible existence of the so-called 'extinction contrast' contribution to the dislocation image since we have neglected some intrinsic diffraction properties, such as the variation of the diffraction ability from point to point in the strain fields (Authier 1967; Miltat & Bowen 1975). However, the good agreement between our simulations and the recorded images shows that the direct images of superscrew dislocations consist dominantly of orientation contrast rather than extinction contrast on both back-reflection and transmission topographs.

The geometrical diffraction model is also unable to describe the influence of wavelength on the dislocation images, but it reveals a more important factor, the sample-to-film distance, that dominantly determines the image dimensions. This can be explicitly verified from the fact that the image dimension significantly increases on a series of synchrotron topographs taken at a fixed Bragg angle (i.e. fixed wavelengths) but at increasing sample-to-film distances. Such a phenomenon has been observed by Tanner *et al*. (1977) and is confirmed by our detailed measurements. Since the variation of the sample-to-film distance alone can explain the corresponding variation of the image dimensions, we can infer that the influence of wavelength is insignificant compared with the influence of the sample-to-film distance.

Compared with superscrew dislocations, ordinary dislocations with small Burgers vectors have much smaller strains, and the wavelength spread is accordingly much narrower. Therefore, although we have focused on the superscrew dislocation images in the above sections, the significant dependency of dislocation images on the sample-to-film distance is also applicable for ordinary dislocations (Dudley *et al*. 1999). For

example, the basal plane dislocations in 6H–SiC are generally $\frac{1}{3}\langle 11\bar{2}0\rangle$ dislocations ($|\boldsymbol{b}| \simeq 3$ Å) which are equivalent to the $\frac{1}{2}\langle 110\rangle$ dislocations in silicon. As can be seen from figures 8*a*, *b*, the images of these dislocations are again much wider on the synchrotron topograph than on the Lang topograph, which indicates that the ordinary dislocations have similar contrast mechanisms as superscrew dislocations. The images of ordinary dislocations on high-energy synchrotron topographs (such as those taken at the European Synchrotron Radiation Facility (Zontone *et al*. 1996)) are even wider than on topographs recorded by old synchrotrons. We believe that it is mainly the long sample-to-film distances (20–100 cm), which are necessary because of the small Bragg angles, that lead to the wide dislocation images.

In summary, we have demonstrated that the geometrical diffraction model can be used to describe dislocation images on both characteristic radiation and synchrotron radiation topographs. It is revealed that in characteristic radiation topography, it is the finite spectrum width rather than the divergence of the incident beam that plays an essential role in the formation of dislocation contrast. Due to such a spectrum width, characteristic radiation diffraction occurring in the deformed lattice of a dislocation also belongs to polychromatic diffraction. Consequently, the contrast formation mechanisms are almost identical to those of synchrotron white-beam topography. As a general rule, the dimensions of dislocation images increase drastically with increasing sample-to-film distances, making the characteristic radiation images recorded at short sample-to-film distances much smaller than the synchrotron radiation images recorded at large distances. Therefore, synchrotron topography is more suitable for studying low-density defects, and, especially, it makes it possible for us to study the details of the wide defect images without using high-resolution X-ray plates (such as nuclear emulsion plates). Correspondingly, characteristic radiation topography can be used to reveal defects of relatively higher density in single crystals.

This work was supported by DARPA/AFWL under grant no. F33615-95-C-5426 and by the US Army Research Office under grant nos DAAH04-94-G-0091, DAAH04-94-G-0121 and DAAG55-98-1-0392. The synchrotron experiments were carried out at Beamline X-19C at the National Synchrotron Light Source, Brookhaven National Laboratory, which is supported by the US Department of Energy, under contract no. DE-AC02-76CH00016. The authors are grateful to Dr W. M. Vetter for his assistance in recording the topographs.

References

Authier, A. 1967 *Adv. X-ray Analysis* **10**, 9–31.

Deutsch, M. & Hart, M. 1982 *Phys. Rev.* B **26**, 5558–5567.

Dudley, M., Wang, S., Huang, W., Carter Jr, C. H., Tsvetkov, V. F. & Fazi, C. 1995 *J. Phys.* D **28**, A63–A68.

Dudley, M., Huang, X. R. & Huang, W. 1999 *J. Phys.* D **32**, A139–A144.

Epelboin, Y. 1985 *Mater. Sci. Engng* **73**, 1–43.

Epelboin, Y. 1996 *J. Appl. Crystallogr.* **29**, 331–340.

Huang, X. R., Dudley, M., Vetter, W. M., Huang, W., Wang, S. & Carter Jr, C. H. 1999*a* *Appl. Phys. Lett.* **74**, 353–355.

Huang, X. R., Dudley, M., Vetter, W. M., Huang, W., Si, W. & Carter Jr, C. H. 1999*b* *J. Appl. Crystallogr.* **32**, 516–524.

Klapper, H. 1991 *Crystals: growth, properties and applications* (ed. N. Karl), vol. 13, pp. 109–162. Springer.

Miltat, J. E. & Bowen, D. K. 1975 *J. Appl. Crystallogr.* **8**, 657–669.

Schulz, L. G. 1954 *Trans. Am. Inst. Min. Metall. Pet. Engng* **200**, 1082–1083.

Tanner, B. K. 1996 *X-ray and neutron dynamical diffraction: theory and applications* (ed. A. Authier, S. Lagomarsino & B. K. Tanner), pp. 147–166. New York: Plenum.

Tanner, B. K., Midgley, M. & Safa, M. 1977 *J. Appl. Crystallogr.* **10**, 281–286.

Vetter, W. M. & Dudley, M. 1998 *J. Appl. Crystallogr.* **31**, 820–822.

Zontone, F., Mancini, L., Barrett, R., Baruchel, J., Härtwig, J. & Epelboin, Y. 1996 *J. Synchrotron Rad.* **3**, 173–184.